

## The deep roots of the western Pyrenees revealed by full waveform inversion of teleseismic P waves

Yi Wang et al.

### **Dataset**

We use teleseismic events (Table DR1) recorded by the dense PYROPE transect deployed across the western Pyrenees between October 2012 and October 2013. The transect is composed of 29 CMG40 recording stations, evenly spaced along a 250 km-long profile with a typical inter station spacing around 8 km. We select events with a magnitude larger than 6.0 at epicentral distances comprised between  $30^\circ$  and  $92^\circ$  and keep those with the largest signal-to-noise coming from the different azimuths covered. These criteria led to the selection of five teleseismic events. We estimate the source wavelet of each event by first deconvolving the vertical-component seismograms from the Green's functions computed with the Direct Solution Method (DSM) (Geller and Takeuchi, 1995). The source wavelet is then obtained by computing the first eigenvector of the aligned deconvolved vertical traces.

### **Forward modelling**

Forward and adjoint wave propagations are performed with the DSM/spectral-element method (Komatitsch and Tromp, 1999) hybrid numerical technique described in Monteiller et al. (2013). The principle of this method is to first compute the tractions and displacements produced by the distant teleseismic sources on the edges of a regional 3-D spectral-element grid. We consider impulsive sources with moment tensors taken from the GCMT catalogue (Dziewonski et al., 1981). We then solve regional wave propagation problems with the spectral-element method, imposing the tractions computed in the previous step convolved with the source wavelet as an

input boundary condition. The regional spectral-element domain is a chunk of the spherical Earth, with a free surface that includes the topographic relief of the Pyrenees.

### **Full waveform inversion method**

We perform full waveform inversion of both vertical and radial components of teleseismic P wave records, low-pass filtered at 5 s, following the method described in Monteiller et al. (2015). In this first application of our method to real data, we chose not to include the transverse components into the inversion in order to avoid the complexities that may result from the presence of seismic anisotropy. In the same way, since the shear waves that arrive in the coda of the P wave are generated by P-to-S conversions on crustal discontinuities, their propagation distances are extremely short (of the order of a few wavelengths). We can thus safely neglect the effect of attenuation. We consider time windows that start 5 s before the onset of the P wave and end 45 s after. This choice for the length of the time window is dictated by the rather long durations of source wavelets (of the order of 30-40 s, depending on the event) and the necessity to include the contributions of P-to-S conversion and of the first multiples into the inversion. The main difference with the method described in Tong et al. (2014) is that we invert broadband waveforms instead of receiver functions (i.e. components deconvolved from the vertical component). The idea is to retain the long-period components of the seismic wavefield to better constrain long wavelength heterogeneities but also to exploit the vertical-component waveforms.

The tomographic model is parameterized in terms of  $V_p$  and  $V_s$  values in a regular Cartesian grid, with 2 km cubic cells. The starting models are smooth 1-D density,  $V_p$  and  $V_s$  profiles derived from the ak135 reference Earth model (Kennett et al., 1995). For each source we compute the gradient of the waveform misfit function with respect to  $V_p$  and  $V_s$  using the adjoint method (Tromp et al., 2005). We also compute gradients for density, but since their amplitude are negli-

gible compared to those for  $V_p$  and  $V_s$ , the density model is kept constant. We have checked that adding density perturbations in the inversion does not improve the waveform misfit. This suggests that seismic waveforms alone cannot constrain the density model, at least when considering periods longer than 5 s. We solve the non-linear inverse problem with an iterative L-BFGS method (Nocedal and Wright, 2006), starting from the initial smooth 1-D models. The selection of step lengths is performed using the Wolfe conditions, which also provide a stopping criterion (see Monteiller et al. (2015) for more details). The algorithm converges in 9 iterations, reaching a misfit reduction of about 50 %.

Comparisons between real and synthetic seismograms computed in the starting 1-D model and in the final 3-D model are shown in Figs DR1-DR5. Note that to produce these figures the real seismograms have been normalized to a unit maximum amplitude, and that the same normalization has been applied to the corresponding synthetic seismograms. Since the amplitudes on the radial components are 2-3 times smaller than on the vertical component, the radial component is thus amplified compared to the vertical component. In spite of a higher noise level on the horizontal component, the improvement of waveform fits is more important on the radial component because the synthetic radial component computed in the starting smooth 1-D model only contain the contribution of the direct P wave. The final model better explains not only the phase and amplitude of direct P waves but also all the converted and multiply-reflected waves that arrive in the coda of P waves, mainly observed on the radial components. However, not surprisingly, the quality of the fit varies from one event to the other. For example, it is poorest for event 1, which has the smallest magnitude (6.1), while it is best for event 2, which has the largest magnitude (8.3).

### **Resolution test**

In order to infer the spatial resolution given by our waveform dataset, we have performed a synthetic inversion experiment on a checkerboard model. This model consists of a mosaic of alternatively positive and negative 16 % anomalies with respect to a smooth 1-D background medium. The anomalies have an infinite extension along the direction perpendicular to the strike of the seismic profile. The input Vp and Vs models are shown in Figs. DR6A and DR6C, respectively. The synthetic seismograms are computed in the input model, using the source wavelets that were determined for each teleseismic source. This means that both the frequency content of the signals and the path distribution are the same as those in the real data inversion. After 12 iterations of our iterative waveform inversion algorithm, we obtain the final Vp and Vs models shown in Figs. DR6C and DR6D, respectively. The checkerboard pattern is well retrieved down to 60 km depth in both the Vp and Vs models. In spite of a decrease of spatial resolution with depth, our method is capable of retrieving velocity anomalies that are smaller than both P and S wavelengths. In particular, the inversion is able to capture the inversions of the velocity gradient with depth, which would be impossible with classical travel time tomography.

### **Modeling of Bouguer gravity anomalies**

For the modeling of Bouguer gravity anomalies, the Vp model is mapped to density using the relation  $\rho = V_p/3 + 0.60$  (Birch, 1961), where density is in  $\text{g.cm}^{-3}$  and P velocity in  $\text{km.s}^{-1}$ . For mantle rocks we use a constant density of  $3.3 \text{ g.cm}^{-3}$ . Density anomalies (Fig. DR7) are calculated with respect to a reference homogeneous crust with a density of  $2.7 \text{ g.cm}^{-3}$  and a thickness of 35 km. Bouguer gravity anomalies (Fig. DR8) are computed by integrating the contributions of density anomalies along finite-width horizontal line elements (Talwani, 1973). In our computations we consider that the width of the density anomalies in the direction perpendicular to the

seismic profile is 20 km. This width is on par with the size of the Bouguer anomaly observed in the Mauléon basin.

## References

- Birch, F., 1961, The velocity of compressional waves in rocks to 10 kilobars, Part 2: *Journal of Geophysical Research*, v. 66, 2199–2224.
- Diewonski, A. M., Chou, T. A., and Woodhouse, J. H., 1981, Determination of earthquake source parameters from waveform data for studies of global and regional seismicity: *Journal of Geophysical Research*, v. 86, 2825–2852.
- Geller, R. J., and Takeuchi, N., 1995, A new method for computing highly accurate DSM synthetic seismograms: *Geophysical Journal International*, v. 123, 449–470.
- Kennett, B. L. N., Engdahl, E. R., and Buland, R., 1995, Constraints on seismic velocities in the Earth from travel times: *Geophysical Journal International*, v. 122, 108–124.
- Komatitsch, D., and Tromp, J., 1999, Introduction to the spectral-element method for 3-D seismic wave propagation: *Geophysical Journal International*, v. 139, 806–822.
- Monteiller, V., Chevrot, S., Komatitsch, D., and Fuji, N., 2013, A hybrid method to compute short- period synthetic seismograms of teleseismic body waves in a 3-D regional model: *Geophysical Journal International*, v. 192, 230–247.
- Monteiller, V., Chevrot, S., Komatitsch, D., and Wang, Y., 2015, Three-dimensional full waveform inversion of short-period teleseismic wavefields based upon the SEM-DSM hybrid method: *Geophysical Journal International*, v. 202, 811–827.
- Nocedal, J., and Wright, S., 2006, *Numerical optimization*, Springer, New York, USA.

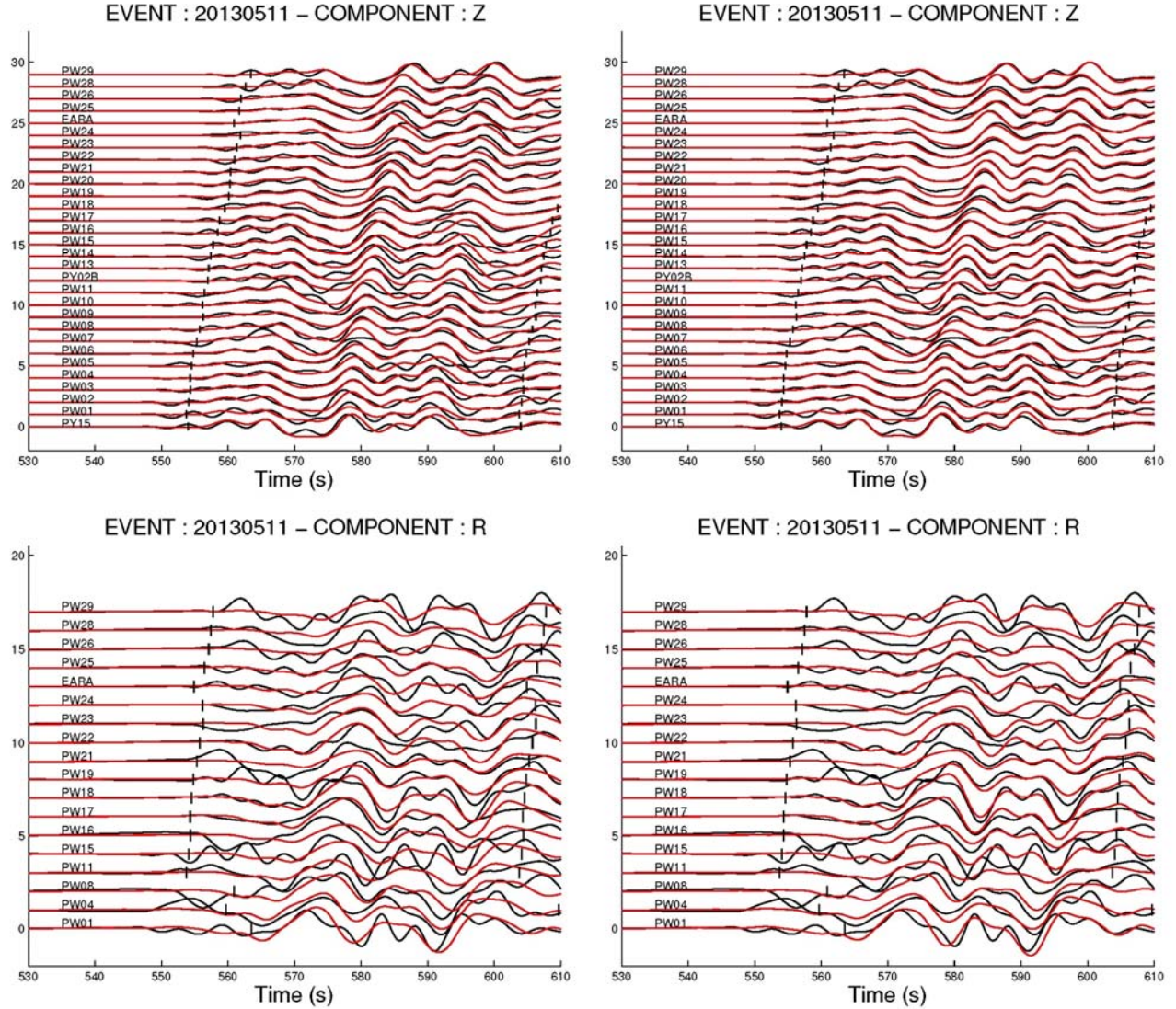
Talwani, M., 1973, Methods in Computational Physics, vol. 13, chap. Computer usage in the computation of gravity anomalies, pp. 344–389, Academic Press.

Tong, P., Chen, C., Komatitsch, D., Basini, P., and Liu, 2014, Q., High-resolution seismic array imaging based on an SEM-FK hybrid method: Geophysical Journal International, v. 197, 369-395.

Tromp, J., Tape, C., and Liu, Q. Y., 2005, Seismic tomography, adjoint methods, time reversal and banana-doughnut kernels: Geophysical Journal International, v. 160, 195–216.

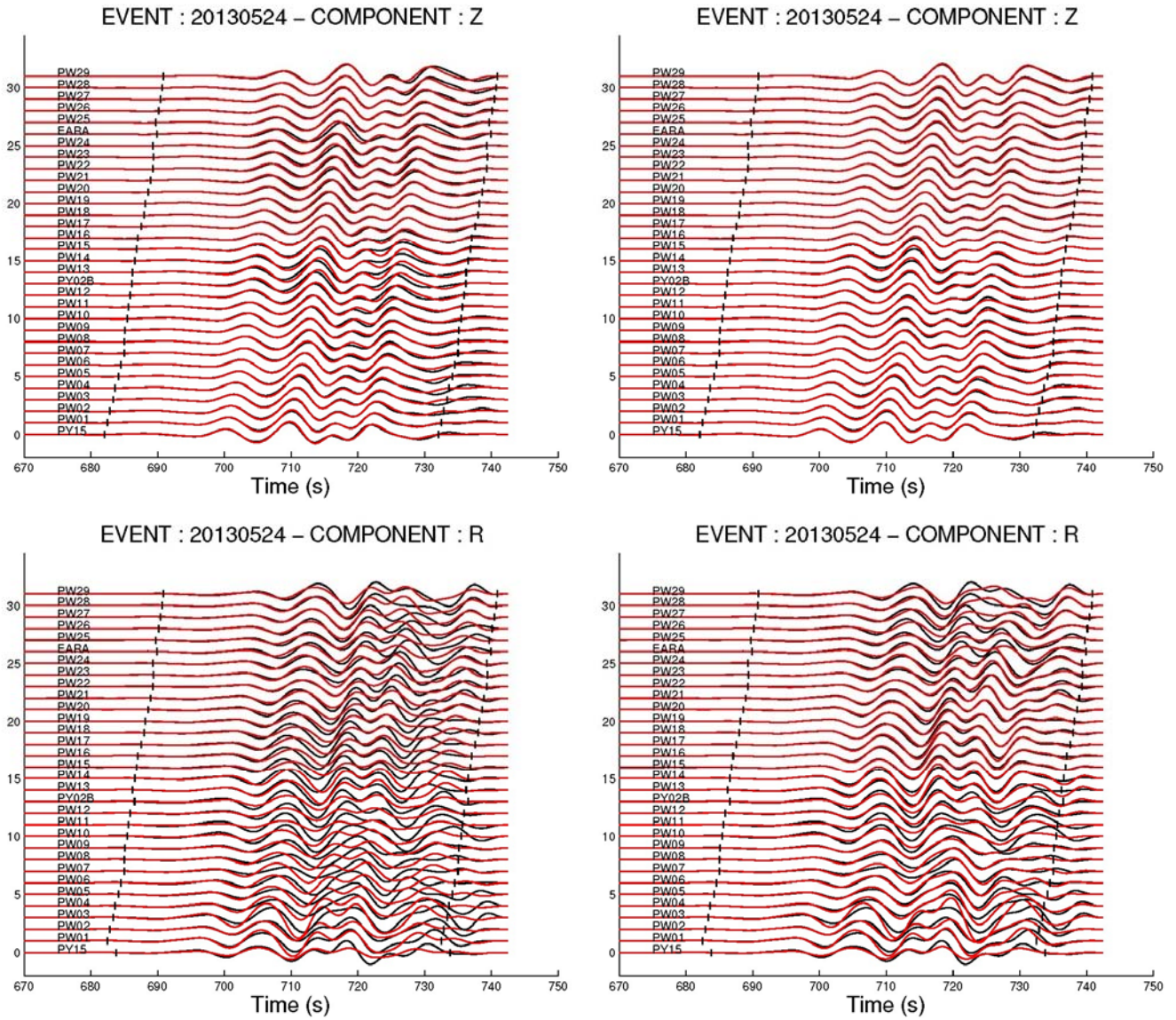
Event	Origin Time	Latitude (deg.)	Longitude (deg.)	Depth (km)	Mw
1	11/05/2013 02:08:08.5	+26.56	+57.77	15	6.1
2	24/05/2013 05:44:49.6	+54.87	+153.28	609	8.3
3	13/08/2013 15:43:15.2	+5.77	-78.20	12	6.7
4	30/08/2013 16:25:02.3	+51.54	-175.23	29	7.0
5	25/09/2013 16:42:43.2	-15.84	-74.51	40	7.1

Table DR1: List of the five teleseismic events used in this study. The origin times and locations are from the USGS catalogue (<http://earthquake.usgs.gov/earthquakes/search/>).



**Figure DR1.** Observed (black lines) and synthetic (red lines) seismograms for event 1. Top: Vertical component. Bottom: Radial Component. The vertical black marks represent the limits of the time windows that are used in the waveform inversion. Left: Synthetic seismograms computed in the smooth initial 1-D model. Right: Synthetic seismograms computed in the final 3-D model.





**Figure DR2.** Same as Fig. DR1 but for event 2.



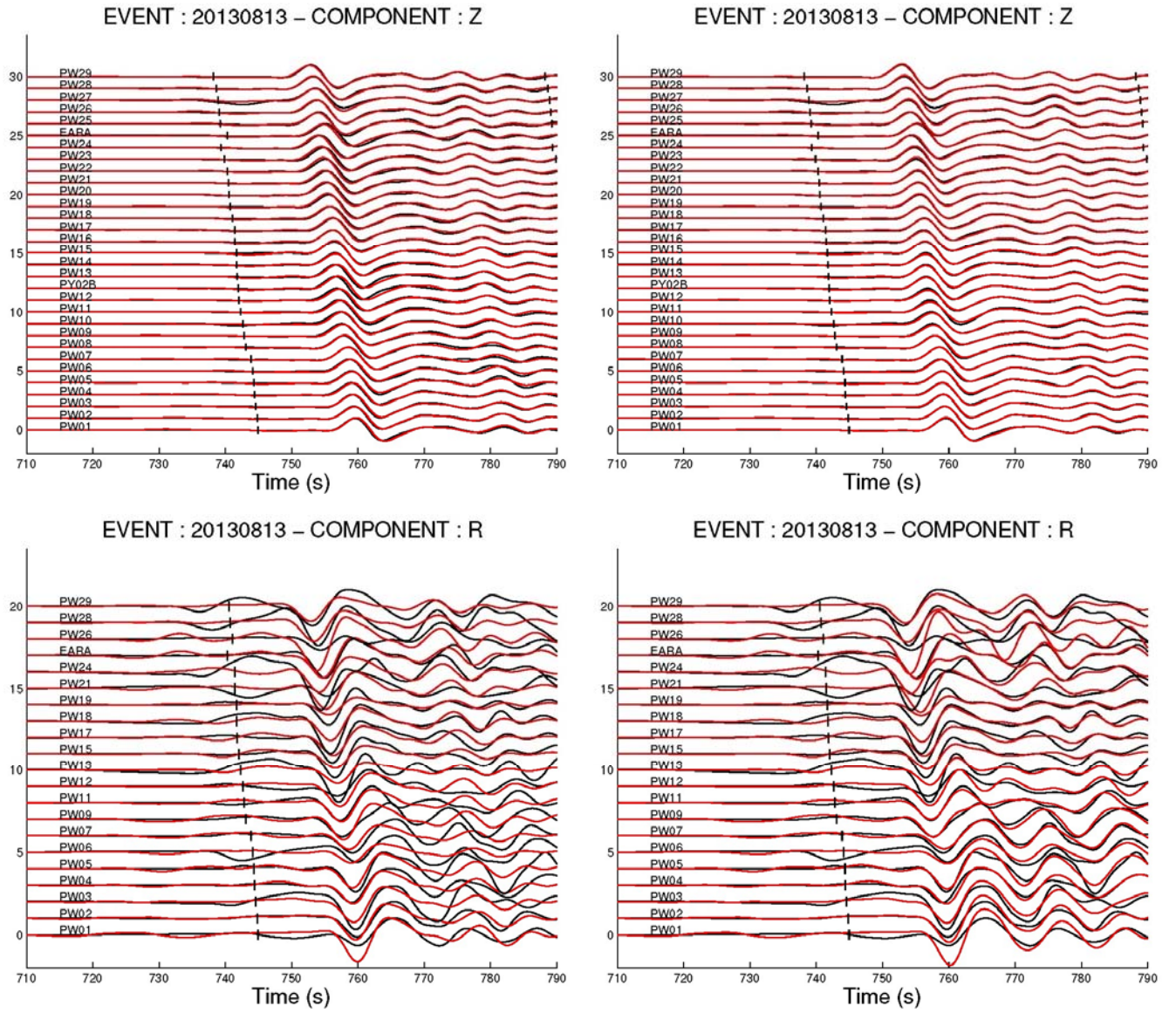


**Figure DR3.** Same as Fig. DR1 but for event 3.

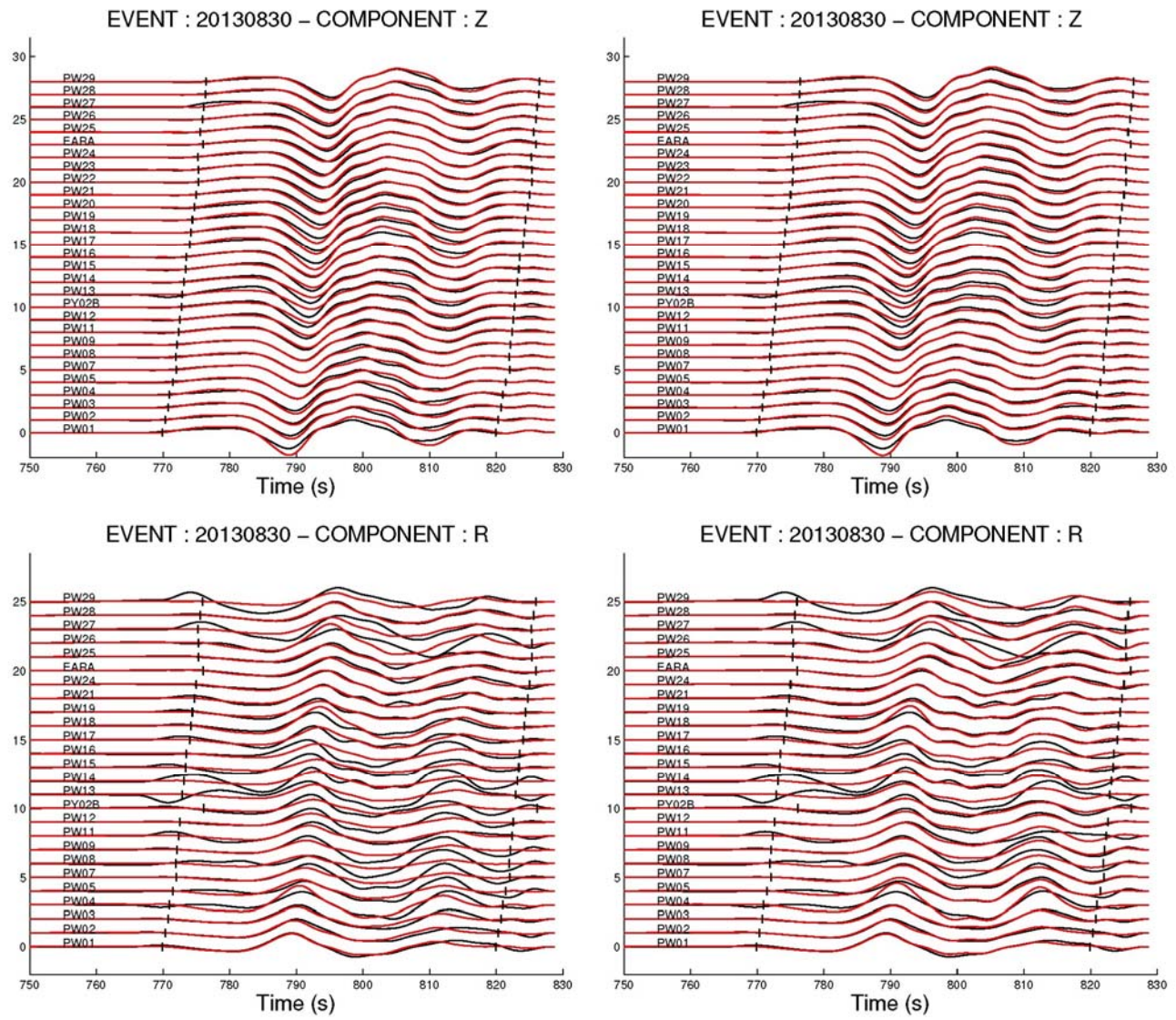


**Figure DR4.** Same as Fig. DR1 but for event 4.



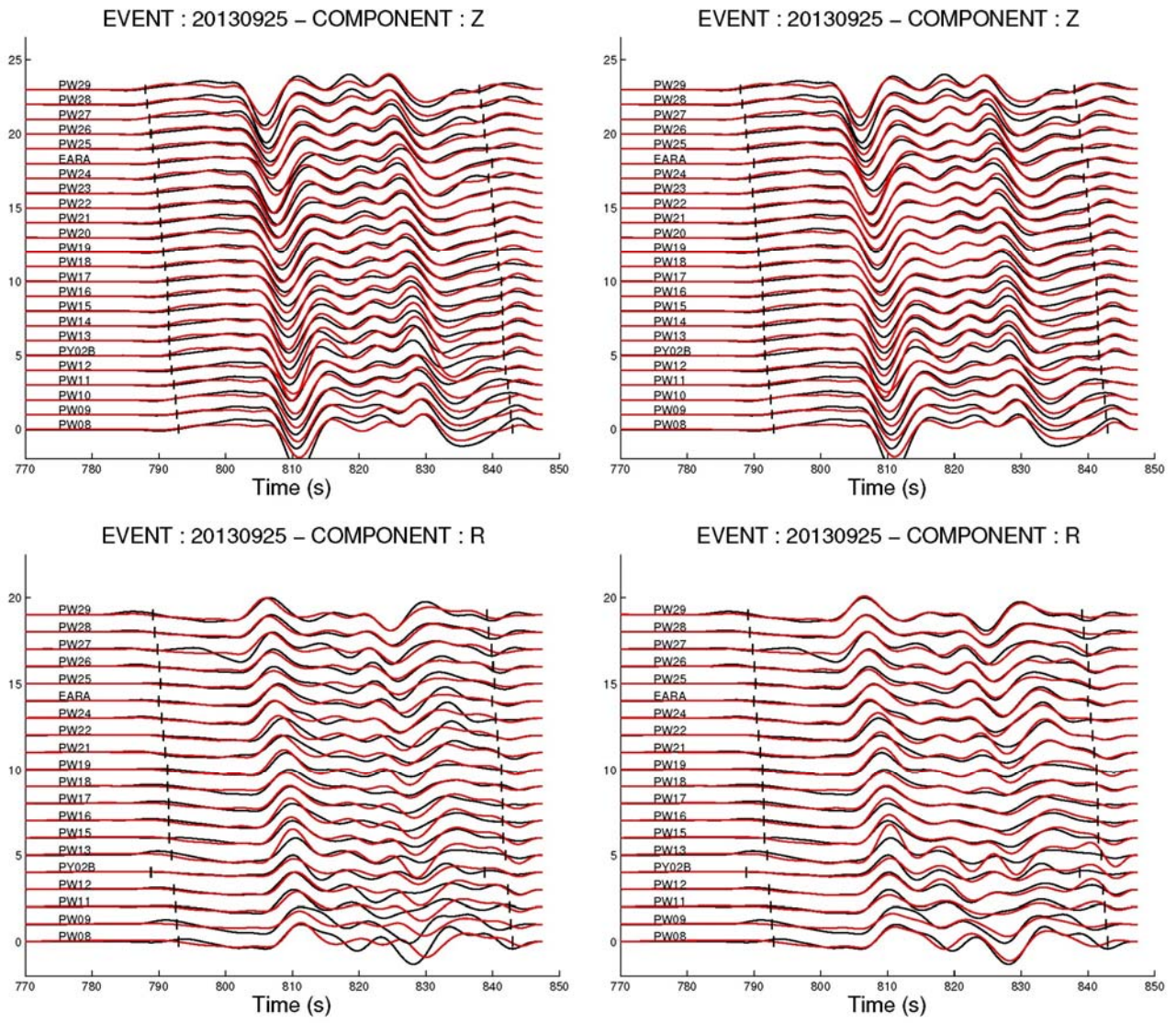


**Figure DR5.** Same as Fig. DR1 but for event 5.

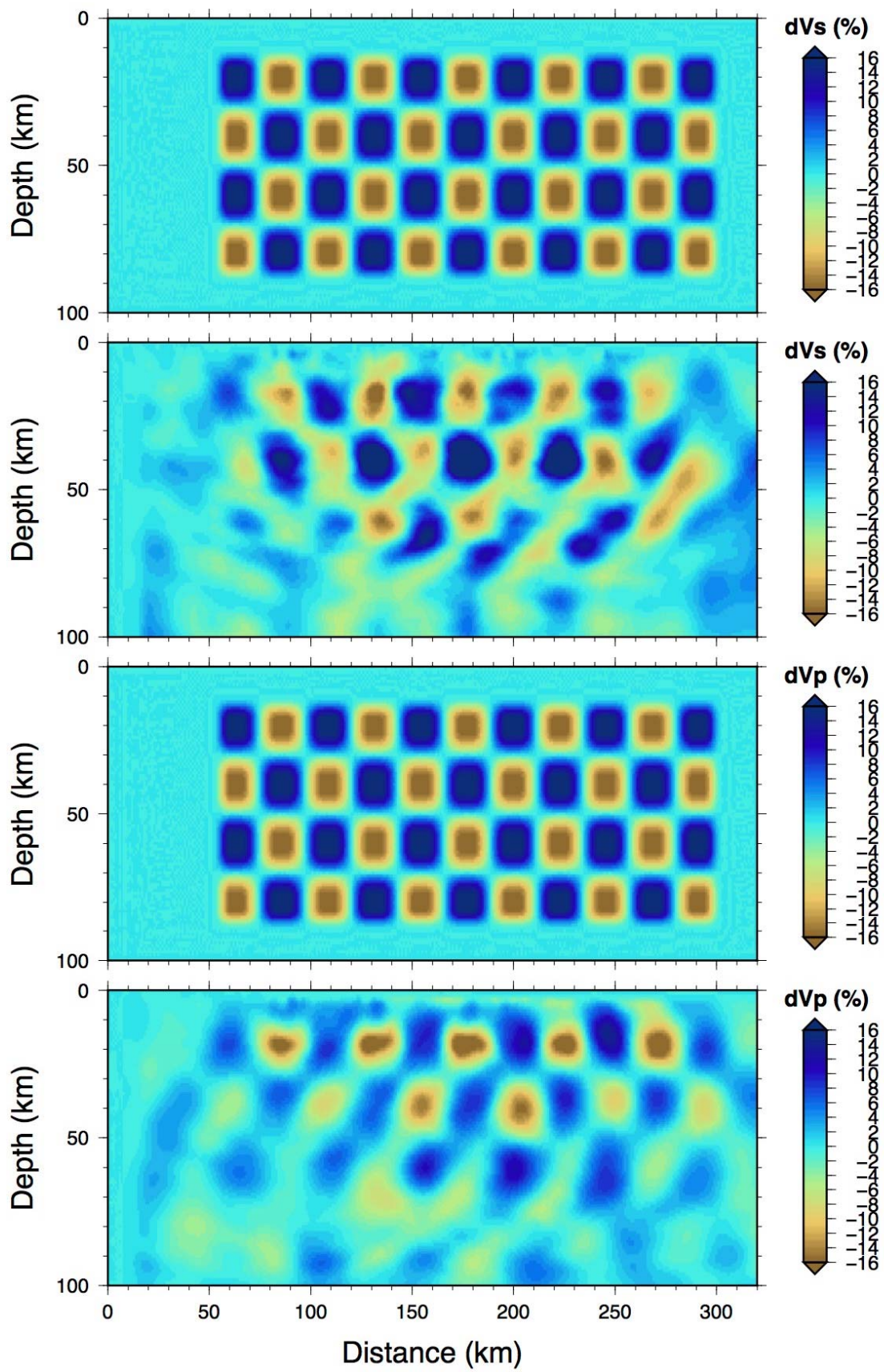


**Figure DR6.** Results of the synthetic checkerboard inversion test. The figure shows the input Vp (D) and Vs (B) models, and the output Vp (C) and Vs (A) models.



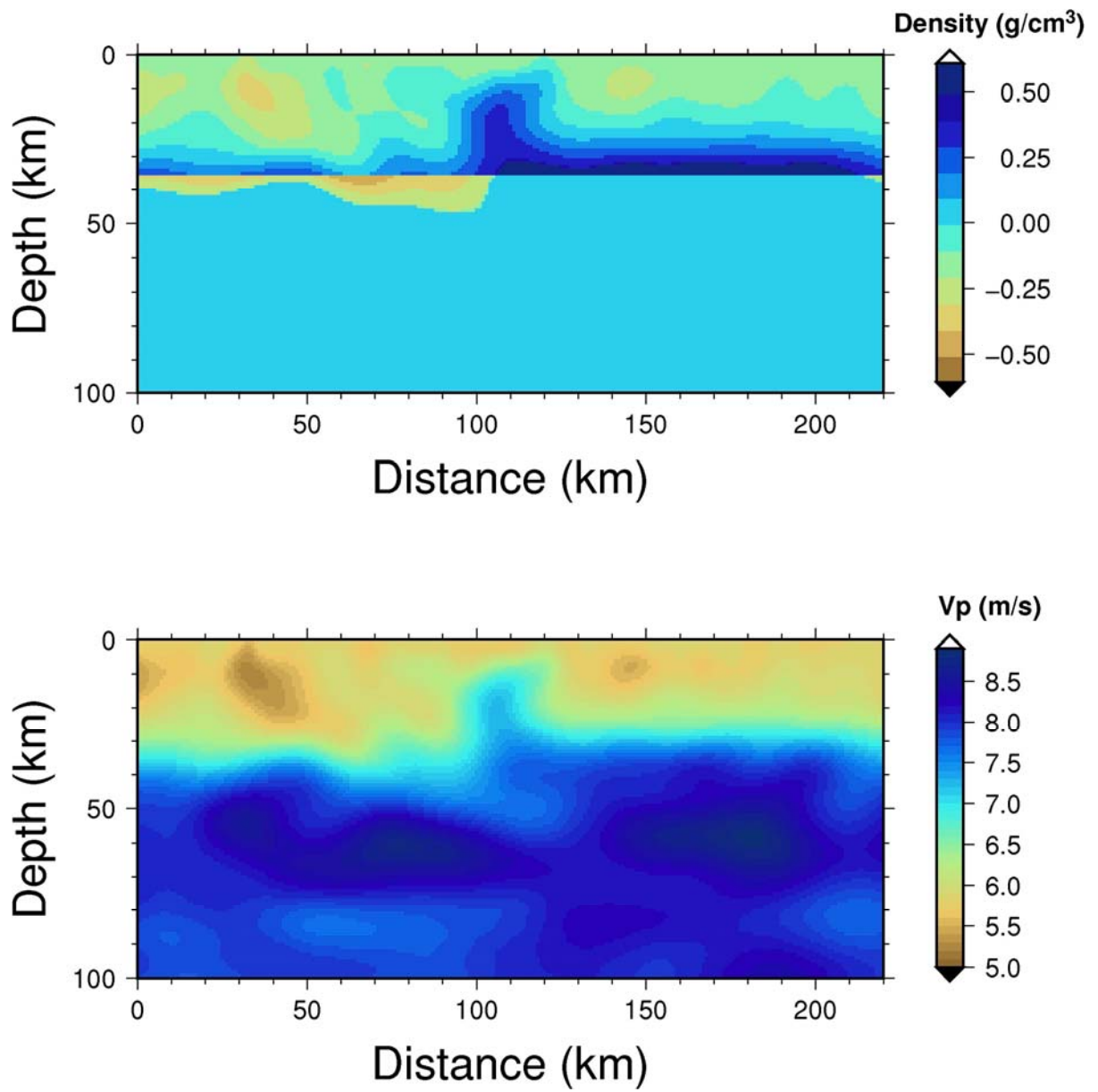


**Figure DR7.** Model of density anomalies (top) derived from the P wave speed model (bottom).

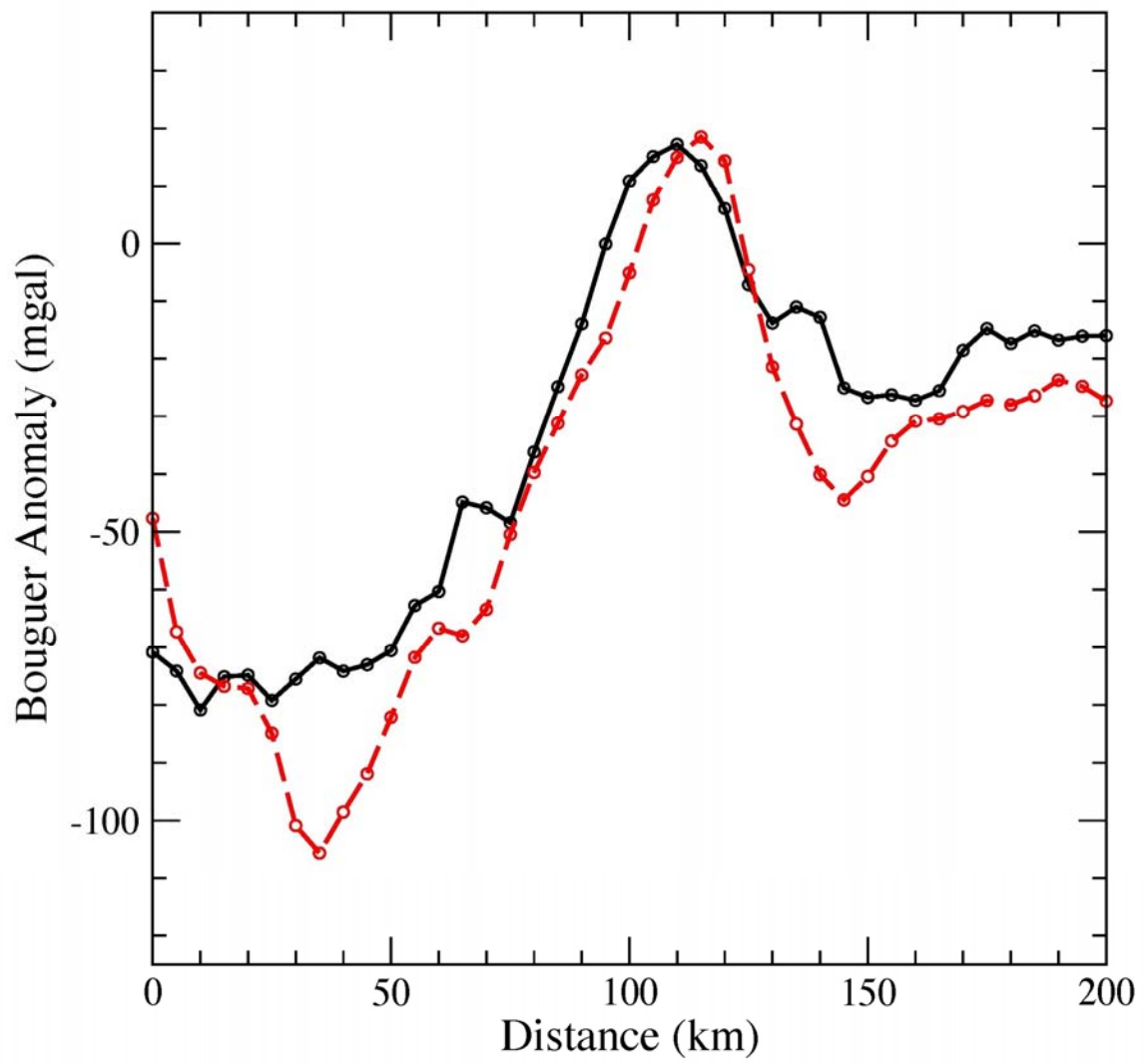


**Figure DR8.** Computed (red dashed line) and observed (black solid line) Bouguer gravity anomalies.